Radially Polarized, Half-Cycle, Attosecond Pulses from Laser Wakefields through Coherent Synchrotron Radiation

F. Y. Li[1], Z. M. Sheng[1,2],* M. Chen[1], L. L. Yu[1], J. Meyer-ter-Vehn[3], W. B. Mori[4], and J. Zhang[1]
[1] *Key Laboratory for Laser Plasmas (MoE), Department of Physics and Astronomy, Shanghai Jiao Tong University, Shanghai 200240, China*
[2] *SUPA, Department of Physics, University of Strathclyde, Glasgow G4 0NG, UK*
[3] *Max-Planck-Institut für Quantenoptik, D-85748 Garching, Germany*
[4] *University of California, Los Angeles, California 90095-1547, USA*
(Dated: May 7, 2014)

Attosecond bursts of coherent synchrotron-like radiation are found when driving ultrathin relativistic electron disks in a quasi-one-dimensional regime of wakefield acceleration, in which the laser waist is larger than the wake wavelength. The disks of overcritical density shrink radially due to the focusing wake fields, thus providing the transverse currents for the emission of an intense, radially polarized, half-cycle pulse of about 100 attoseconds in duration. The electromagnetic pulse first focuses to a peak intensity 10 times larger ($7 \times 10^{20}\mathrm{W/cm^2}$) than the driving pulse and then emerges as a conical beam. Saturation of the emission amplitudes is derived analytically and in agreement with particle-in-cell simulation. By making use of gas targets instead of solids to form the ultrathin disks, the new scheme allows for high repetition rate required for applications.

PACS numbers: 52.38.Kd, 52.59.-f, 52.59.Ye, 42.65.Ky

arXiv:1401.2799v2 [physics.plasm-ph] 6 May 2014

Great efforts have been devoted to obtain extreme-ultraviolet (XUV) and soft X-ray pulses having attosecond duration. They open the door to attosecond spectroscopy of bound electrons [1]. An established method to produce such pulses relies on atomic harmonics excited by ultrafast lasers at an intensity below 10^{16} $\mathrm{W/cm^2}$ [2]. Harmonics from solid surfaces [3] make use of relativistic optics ($>$ 10^{18} $\mathrm{W/cm^2}$) [4] and allow for much brighter sources. Single attosecond spikes can be isolated from trains of pulses by means of high-pass filters [5]. By temporally rotating either the surface geometry [6] or the driver wavefront [7], individual attosecond pulses can be obtained even without filtering.

In this Letter, we follow a different path, producing intense isolated attosecond pulses from underdense plasmas rather than solids. With gas targets the condition of ultrahigh laser contrast is greatly relaxed, and a bright source allowing for high repetition rate may become possible. The new path is based on wakefield acceleration driven by an intense short laser pulse. As it is well known, these relativistic plasma waves exhibit strong accelerating and focusing fields for electrons. They promise acceleration to high energies over a short distance [8]. Often the laser beam is tightly focused to reach highest possible intensity I_0 with waist $W_0 \leq \sqrt{a_0}\lambda_p/\pi$, where λ_p is the plasma wavelength and $a_0 = 8.5 \times 10^{-10}\lambda_0[\mu\mathrm{m}]\sqrt{\mathrm{I_0[W/cm^2]}}$ the normalized laser amplitude at wavelength λ_0. Plasma electrons are then pushed sideways by the light pressure, creating bubble-like wakes. Some electrons circling around the bubble are transversely injected at the rear vertex and then accelerated forming a narrow bunch [9]. This is known as the bubble regime of wakefield acceleration [10]. An important feature is that the accelerating bunch oscillates in the wake forced by the focusing fields and emits bright betatron radiations [11].

Here we make use of a different regime of wakefield acceleration, occurring for laser waists larger than wake wavelength. Wake electrons now perform mainly one-dimensional (1D) longitudinal motion due to weak radial expelling. The density wave crests show disk-like profiles as visualized in experiments [12]. Most notably, they compress into dense sheets when driven close to wavebreaking. Actually such ultrathin wave crests have been used as relativistic mirrors to backscatter femtosecond probe pulses [13]. In this way, attosecond XUV/X-ray pulses are obtained owing to simultaneous frequency upshift and pulse shortening by Dopper factors of $\sim 4\gamma_p^2$, where $\gamma_p = 1/\sqrt{1 - v_p^2/c^2}$ with v_p the wake's phase velocity and c the light speed in vacuum. In this work, however, we follow another line that does not require a second pulse, but leads to self-emission of a bright attosecond pulse from the dense electron sheet itself. For this to happen, the electron sheet has to be injected and accelerated in the wakefield. Different from the ultrathin density crest belonging to the quasi-1D waveform [13], the injected sheet contracts in transverse direction due to the focusing wake fields, while boosted at the same time in energy by wakefield acceleration. The central new result of this Letter is that a strong unipolar attosecond pulse is produced by the transverse currents formed during the contraction motion. This coherent attosecond source is also in contrast to the incoherent femtosecond betatron X-rays normally obtained so far [11].

Different ways may be used to induce injection of such electron sheets [14]. A simple method has been described using an up-ramp density profile followed by a plateau [15]. Wavebreaking then occurs at the transition point and leads to a sudden longitudinal injection into the quasi-1D wake, different from the continuous transverse injection in the bubble regime [9, 10]. The key point is that, along the ramp, the wave crest travels at superluminal speed, preventing premature injection. At the transition to the plateau, the density spike is injected as a whole due to fast switching of v_p. It forms an ultrathin (few nm) overcritical dense electron disk that accel-

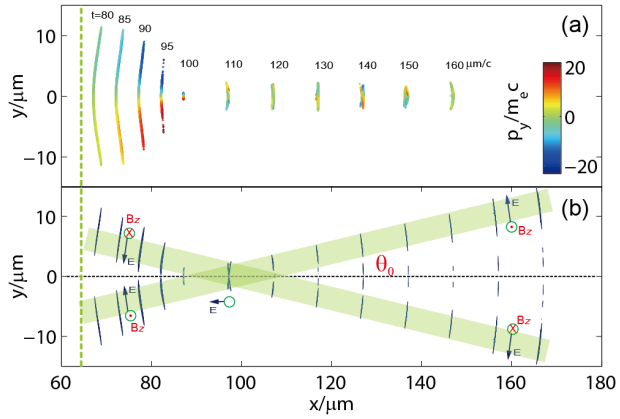

FIG. 1: (Color online). (a) Snapshots of trapped electron sheet at different times (given as label) and colored according to transverse momentum p_y and (b) the radiated attosecond emission given as contour plot of B_z^2. The dashed line on the left side marks the point of wavebreaking and injection into the wake. The full density pattern of the wake is given in Fig. 2(b) for $t = 160\ \mu$m/c. These results are obtained from 2D PIC simulation in x-y space. In full 3D geometry the emission appears as an annular beam propagating as a radially polarized, half-cycle, attosecond (RHA) pulse along a cone with opening angle $\theta_0 \sim 10^\circ$, indicated as shaded stripes.

erates in the wakefield.

The evolution of an electron sheet in the wakefield and the associated radiation flash are first illustrated in Figs. 1(a) and 1(b). It is seen that the sheet contracts transversely to a smallest diameter in tens of laser periods after injection, while accelerating longitudinally up to a highly relativistic γ-value (compare Fig. 3). It is in this short time interval that the attosecond pulse is emitted. As found in Fig. 1(b), the pulse is first attached to the electron sheet, but then propagates along a cone, while the electrons move closer to the axis in a channel of almost constant diameter.

These results are obtained from two-dimensional particle-in-cell (2D PIC) simulations [16]. Here in order to control trapping of the electron sheet, the self-injection method with particular density tailoring was employed [15]. A linearly polarized (along z direction), 18 fs (full width at half maximum) laser pulse of peak intensity $I_0 = 7.7 \times 10^{19}$ W/cm^2 irradiates an underdense plasma slab with a 65μm-long ramping front edge. The plateau density is $n_0 = 0.04 n_c$ with $n_c = 1.74 \times 10^{21}$ cm^{-3} the critical density for $\lambda_0 = 0.8\ \mu$m. A laser waist of $W_0 = 17\ \mu$m is enough for the formation of wide sheets in the quasi-1D regime. In the simulation, 158×25 grids cells per μm^2 were used and sufficient to resolve the attosecond spikes; even higher resolutions gave almost the same results. Furthermore, an initial electron temperature of $T_e = 20$ eV was chosen to mimic field ionization by prepulse.

We now discuss the radiation process in general. The injected electrons are diverted by the focusing wake fields toward the central axis according to $d\beta_\perp/dt \simeq \varepsilon_\perp/\gamma$. Here $\beta_\perp$ is the normalized transverse velocity; t and the focusing field $\varepsilon_\perp$ have, respectively, been normalized by ω_0^{-1} and $E_0 = m_e\omega_0 c/e$ with electron mass m_e, elementary charge e and laser frequency $\omega_0 = 2\pi c/\lambda_0$. Near the central axis, the focusing field, $\varepsilon_\perp \propto n_0 r$, is almost linear in radius r and the ambient density n_0. Trapped electrons then perform synchrotron-like motion with curvature radius $\rho \simeq \lambda_0\gamma/(2\pi\varepsilon_\perp)$ and emit broadband radiation with cutoff frequency $\omega_c \simeq 3\gamma^3 c\rho^{-1}$ [17]. However, there are a couple of new features when compared with bubble betatron radiation [11]. First, the high density of the sheet, typically larger than 10^{21} cm^{-3} [15], enables synchrotron emission in a coherent manner. Coherence occurs provided that a sufficiently large number of electrons resides in a volume with scale length equal to the radiation wavelength in the rest frame of electrons. For the present case, it requires the sheet density to satisfy $n_s \gg 10^{13}\varepsilon_\perp^3\gamma^4$ cm^{-3}, where radiation at the cutoff wavelength $\lambda_c = 2\pi c/\omega_c$ is assumed. Considering $\varepsilon_\perp \sim 0.1$, this criteria is readily met even for $\gamma > 100$. Second, due to axial symmetry and inward acceleration of the disk electrons, a radially polarized half-cycle electromagnetic pulse is emitted. Third, with the increase of γ by wakefield acceleration, the radiated power grows $\propto \gamma^2$ [17]. That means the dominant emission profile roughly overlaps the sheet during amplification, having an attosecond duration. It is worth noting that similar radially polarized pulses have actually been detected from thin photoconductors, where annular microelectrodes induced the radial current [18]. Due to the static wafer plane, however, only pulses of picosecond duration were observed, determined by the lifetime of the radiating current.

These features are well illustrated in the sample simulation. Figure 2(a) records how the peak field B_z^{max}/B_0 of the radially polarized, half-cycle, attosecond (RHA) pulse evolves; $B_0 = m_e\omega_0/e$ is the normalizing field. According to Fig. 1(b), the pulse emerges in three stages: pulse generation during initial sheet contraction, beam crossing on axis, and finally annular beam propagating along a cone. At the phase of crossing, the emission focuses to a maximum of $B_z^{max}/B_0 \geq 18$, as found in the shaded region of Fig. 2(a). This corresponds to a peak intensity greater than 7×10^{20} W/cm^2. After complete separation ($t \sim 130\ \mu$m/c), the actual peak field shows up as $B_z^{max}/B_0 = 4.5$, corresponding to 4.3×10^{19} W/cm^2. Importantly, Fig. 2(b) shows how the RHA pulse propagates at later time. The initial quasi-1D wake is evolving into a complex broken-wave pattern due to laser evolution [19]. The half-cycle pulse as short as 120 as (see Fig. 2(c)) is propagating inside the wake but deviated from the axis. It contains a broadband XUV spectrum extending up to $\sim$ 40 eV in photon energy. In the present case, the annular beam carries a total energy of 12 mJ, which is $\sim 2 \times 10^{-3}$ of the incident laser energy. The radial polarization of the attosecond pulse is confirmed in Fig. 2(c), where switching polarization of the driving pulse from y to z direction has almost no effect on the emission profile. We have checked that the annular beam is uniform azimuthally when obtained in 3D simulation.

The basic dynamics of RHA generation can be derived from a simplified model. It assumes that a flat, monoen-

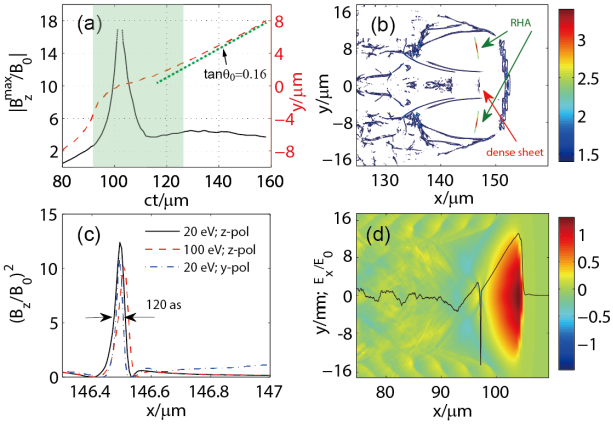

FIG. 2: (Color online). (a) Evolution of peak field $|B_z^{max}|/B_0$ (solid) and associated y coordinate (dashed) of the RHA pulse versus time. The shaded region refers to the crossing stage as explained in the text. The green dotted line indicates the slope of propagation direction. (b) Contour plots of the electron density n/n_c plus $|B_z/B_0|$ (share the same color bar) at $t = 160\ \mu$m/c. At this late time, the wake has developed a complex pattern, in particular to the sides bordering unperturbed plasma and downstream. The only features relevant to this Letter are the tiny dense sheet of relativistic electrons (marked by red arrow) and the RHA pulse (marked by green arrows). (c) Line-outs of $(B_z/B_0)^2$ along $y = 8.32\ \mu$m at $t = 160\ \mu$m/c for three cases corresponding to different initial plasma temperatures (20 and 100 eV) and y or z polarization of driving laser pulse. (d) Snapshot of the longitudinal electric field E_x at $t = 110\mu$m/c; black curve ($\times 10$) shows line-out along central axis.

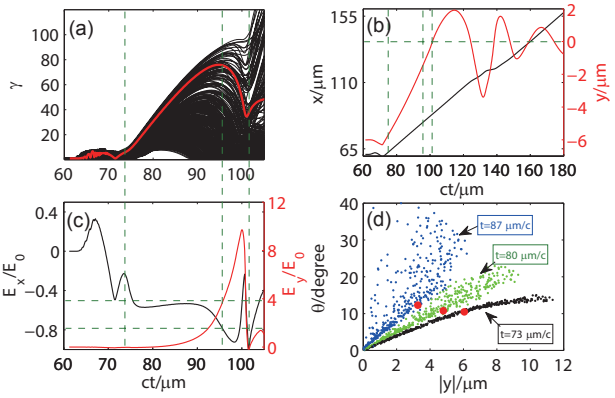

FIG. 3: (Color online). Particle tracking of 400 uniformly distributed electrons picked from the lower half of the sheet at $t = 80\mu$m/c. (a) Their γ factors versus time. The red curve highlights a typical electron which was initially located near the center of the lower half and belongs to the most energetic ones after acceleration. Time histories are presented for this electron in terms of (b) its coordinates and (c) the electric fields E_x and E_y felt by it. The vertical dashed lines (from left to right) marks, respectively, the time of injection, γ saturation and reaching $y = 0$. (d) Distributions of the propagation angle $\theta \simeq (180^\circ/\pi)\arctan\beta_y$ for these electrons versus $|y|$ at the times indicated; $t = 73\ \mu$m/c corresponds to just before injection. The red dots refer to the typical electron defined in (a).

ergetic electron sheet of delta-like density profile $n_s = \delta(x/\sigma_s)$ with finite areal density $\sigma_s = \int n_s dx$ and no initial transverse momentum is injected into a wakefield of uniform accelerating and focusing fields. Coherent radiation from the electron sheet is described by the 1D wave equation $(\partial^2/\partial x^2 - c^{-2}\partial^2/\partial t^2)E_{y,r} = \epsilon_0^{-1}c^{-2}\partial J_{y,r}/\partial t$, where $J_{y,r} = -ec\beta_{y,r}n_s$ is the radiating current with $\beta_{y,r} = \int_{\tau_0}^{\tau_1} d\beta_y \ll 1$ the velocity integrated over a short transverse acceleration [20]. The radiated field $E_{y,r}$ is first calculated in the rest frame of the sheet with Lorentz factor $\sim\gamma$ and then transformed to the laboratory frame; the result is given by

$$E_{y,r} \simeq (\frac{\sigma_s}{\epsilon_0})\beta_{y,r}^R\gamma, \qquad (1)$$

where $\beta_{y,r}^R$ denotes the velocity $\beta_{y,r}$ in the rest frame. Equation (1) indicates that the radiated power grows $\propto |E_{y,r}|^2 \propto \gamma^2$, while γ follows from $d\gamma/dt = -\vec{\beta}_x\cdot\vec{E}_x - \vec{\beta}_y\cdot\vec{E}_y$. Taking into account the radiated field $E_{y,r}$, the total fields can be expressed as $\vec{E}_x = \vec{E}_{x,w}$ and $\vec{E}_y = \vec{E}_{y,w} + \vec{E}_{y,r}$, where $\vec{E}_{x,w}$ and $\vec{E}_{y,w}$ are the longitudinal and transverse wake fields, respectively. Inserting the expression of Eq. (1), the energy equation reads

$$\frac{d\gamma}{dt} + \frac{\sigma_s}{\epsilon_0}\beta_{y,r}^R\beta_y\gamma - \beta_y E_{y,w} - \beta_x E_{x,w} = 0. \qquad (2)$$

Assuming $\gamma(t=0) = 1$ initially, wakefield acceleration first boosts the γ-value rapidly, which then saturates due to radiation damping at a rate $(\sigma_s/\epsilon_0)\beta_{y,r}^R\beta_y$. Saturation occurs for $\vec{\beta}_x\cdot\vec{E}_x + \vec{\beta}_y\cdot\vec{E}_y = 0$, leading to the saturated field

$$E_{y,r}^{sat} \simeq (E_{x,w}/\tan\theta + E_{y,w}), \qquad (3)$$

where $\tan\theta = \beta_y/\beta_x$ is evaluated at the saturation instant.

It is clear that wakefield acceleration has played an essential role in the attosecond pulse generation. This marks a most prominent feature of the present scheme. Equation (3) suggests that $E_{y,r}^{sat}$ can be large provided that $\tan\theta \simeq \beta_y$ is small initially and the saturated level can be maintained for a long period. There are a couple of other effects not yet included. For the sample case, the injected sheet is not perfectly flat but slightly curved as seen in Fig. 1(a). Due to the sudden longitudinal injection, a curved wake wavefront [12, 13] directly maps into the injected sheet profile and the sheet electrons also inherit finite transverse velocities. These will cause their transverse contraction even without the focusing fields, and the radiation process is ultimately limited by deformation of the sheet profile.

Let us explore these effects by particle tracking. Figure 3 presents the results for a group of electrons uniformly distributed in the lower half of the electron sheet. According to Figs. 3(b) and 3(c), the sheet is injected at $t \simeq 74\ \mu$m/c and focuses to the central axis at $t \simeq 102\ \mu$m/c. During contraction these electrons develop a broad γ spread due to high thermal temperature; see Fig. 3(a). However, the overcritical density and ultrathin feature of the sheet ensure the coherence of the attosecond pulse. It is hardly affected by initial plasma temperatures; results given for $T_e = 10$ eV and 100 eV in Fig. 2(c) show little difference. Moreover, as found in Fig. 3(d),

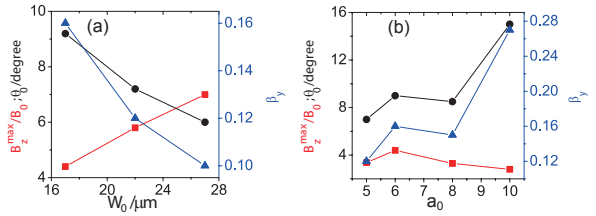

FIG. 4: (Color online). Peak radiation field B_z^{max} (solid square), θ_0 defined in Fig. 1 (solid circle), and β_y of the sublayer emitting the peak field (solid triangle) versus (a) laser waist W_0, while keeping $a_0 = 6$ and $n_0 = 0.04n_c$ fixed, and versus (b) driver amplitude a_0, while keeping $W_0 = 17\mu$m and $n_0 = 0.04n_c$ fixed.

the transverse velocities β_y of the sheet, inherited from wave crest, scale almost linearly with $|y|$ (details see supplemental material) and increase with time due to transverse acceleration. This suggests that the sheet can be subdivided into a sequence of ring-shaped segments defined by their particular β_y. Applying the simplified model to each segment with coordinate frame rotated by angle $\theta \simeq \arctan\beta_y$ from the normal x-y axis, the resulting pointing direction of the radiated electric field will deviate from the y axis; see the schematic drawing in Fig. 1(b). A clear evidence for this is shown in Fig. 2(d), where a sharp negative E_x field shows up at the on-axis overlap joint during beam crossing. Emissions from segments of different β_y then converge due to propagation. This accounts for the focusing effect observed in Fig. 2(a). The finally observed RHA pulse (Fig. 2(b)) builds up from all segment contributions weighted according to Eq. (1). As it turns out, largest contributions stem from ring segments with medium radius. For the present case, the conical angle θ_0 of the radiation peak is measured to be $\tan\theta_0 \simeq 0.16$ in Fig. 2(a). To evaluate this peak field, a typical electron is highlighted in Fig. 3; it is initially located near the center of the lower half and belongs to the most energetic ones after acceleration. According to Eq. (3), the peak field amounts to $E_{y,r}^{sat} \simeq E_x/\tan\theta_0 = 4.7$, which is in fair agreement with the observation of $B_z^{max}/B_0 = 4.5$ after $t \sim 130$ μm/c. Here $E_x \simeq 0.75$ is the longitudinal electric field felt by the electron at the saturation instant and is extracted from Figs. 3(a) and 3(c).

The present RHA generation is robust against changing laser and plasma parameters, provided that they are sufficient to induce the sheet injection. Larger focal spots of the driving pulse generally lead to smaller initial transverse velocities of the injected sheet, generating higher radiation peaks following Eq. (3). This is shown in Fig. 4(a) where B_z^{max} and θ_0 scale almost linearly with W_0. While scanning the laser amplitude a_0 for fixed plasma density $n_0 = 0.04n_c$, an optimal value of $a_0 \sim 6$ exists as seen in Fig. 4(b).

Petawatt lasers, presently coming up, will provide sufficiently high power for the high intensities and the relatively broad focal spots required here. The sample case shown above used a single 350 TW driving pulse delivering 6.5 J in $\sim$ 20 fs. These parameters are well within the ELI-facility capabilities [21] and are also becoming available commercially. The conical angle of the RHA beam is typically less than 10°, thereby allowing refocusing even at half-meter distance by a concentric mirroring tube with diameter less than 16 cm; such techniques have actually been implemented in the measurement of wakefield-based electro-optic shocks [22]. The RHA pulse should also be easily distinguished from other sources due to its radial polarization [23] and hollow pattern.

In conclusion, we have identified novel attosecond bursts of coherent synchrotron radiation from laser wakefield acceleration. The attosecond feature does not derive from an ultrathin solid foil [20] or surface layer [24], but arises from intrinsic features of nonlinear plasma waves, namely steepening and breaking. It makes use of quasi-1D wavebreaking, allowing to trap ultrathin electron sheets in the wakefield. The electron sheet contracts, while boosted in energy, and is found to emit a relativistically intense attosecond pulse. Pulse energy exceeding 10 mJ can be obtained with the laser-to-RHA conversion efficiencies beyond 10^{-3}. Besides being a bright source for attosecond applications, this burst will also provide excellent diagnostics for the wavebreaking dynamics [25] in the quasi-1D regime and corresponding electron sheet generation [15].

ZMS would like to thank the OSIRIS Consortium at UCLA and IST (Lisbon, Portugal) for providing access to OSIRIS 2.0 framework. This work is supported in part by the National Basic Research Program of China (Grant No. 2013CBA01504), the National Science Foundation of China (Grant No. 11121504, 11205101, 11374209 and 11374210), the MOST international collaboration project (Grant No. 2014DFG02330), and the EPSRC, UK. Simulations were performed on Magic Cube at Shanghai Supercomputer Center and Π at Shanghai Jiao Tong University.

* zmsheng@sjtu.edu.cn or zhengming.sheng@strath.ac.uk

[1] F. Krausz and M. Ivanov, Rev. Mod. Phys. **81**, 163 (2009).
[2] P. B. Corkum and F. Krausz, Nat. Phys. **3**, 381 (2007); K. Midorikawa, Jap. J. Appl. Phys. **50**, 090001 (2011).
[3] U. Teubner and P. Gibbon, Rev. Mod. Phys. **81**, 445 (2009).
[4] G. A. Mourou, T. Tajima, and S. V. Bulanov, Rev. Mod. Phys. **78**, 309 (2006); G. Mourou and T. Tajima, Science **331**, 41 (2011).
[5] A. Pukhov, T. Baeva, D. an der Brügge, and S. Münster, Eur. Phys. J. D **55**, 407 (2009); G. D. Tsakiris, K. Eidmann, J. Meyer-ter-Vehn, and F. Krausz, New J. Phys. **8**, 19 (2006).
[6] N. M. Naumova *et al.*, Phys. Rev. Lett. **92**, 063902 (2004).
[7] J. A. Wheeler *et al.*, Nat. Photon. **6**, 829 (2012).
[8] T. Tajima and J. M Dawson, Phys. Rev. Lett. **43**, 267 (1979); E. Esarey, C. Schroeder, and W. Leemans, Rev. Mod. Phys. **81**, 1229 (2009).
[9] I. Kostyukov, E. Nerush, A. Pukhov, and V. Seredov, Phys. Rev. Lett. **103**, 175003 (2009).
[10] A. Pukhov and J. Meyer-ter-Vehn, Appl. Phys. B **74**, 355 (2002); W. Lu *et al.*, Phys. Rev. Lett. **96**, 165002 (2006).
[11] A. Rousse *et al.*, Phys. Rev. Lett. **93**, 135005 (2004); S. Corde *et al.*, Rev. Mod. Phys. **85**, 1 (2013).
[12] N. H. Matlis *et al.*, Nat. Phys. **2**, 749 (2006).

[13] S. V. Bulanov, T. Esirkepov and T. Tajima, Phys. Rev. Lett. **91**, 085001 (2003); A. S. Pirozhkov, *et al.*, Phys. Plasmas **14**, 123106 (2007).
[14] An electron sheet may, in principle, be externally injected into a broad wakefield driven by petawatt lasers. Possible sheet production methods were proposed, for example, in V. V. Kulagin, V. A. Cherepenin, M. S. Hur, and H. Suk, Phys. Rev. Lett. **99**, 124801 (2007); H. C. Wu, J. Meyer-ter-Vehn, J. Fernández, and B. M. Hegelich, Phys. Rev. Lett. **104**, 234801 (2010).
[15] F. Y. Li *et al.*, Phy. Rev. Lett. **110**, 135002 (2013).
[16] R. Fonseca *et al.*, *Lecture Notes in Computer Science*. **2331**, 342-351 (Springer Berlin, Heidelberg, 2002).
[17] T. Shiozawa, *Classical Relativistic Electrodynamics*, Springer-Verlag (Berlin, Heidelberg, 2004), pp77-82.
[18] K. Kan *et al.*, App. Phys. Lett. **102**, 221118 (2013).
[19] J. Xu *et al.*, New J. Phys. **12**, 023037 (2010).
[20] H. C. Wu and J. Meyer-ter-Vehn, Nat. Photon. **6**, 304 (2012).
[21] *ELI-Extreme Light Infrastructure Science and Technology with Ultra-Intense Lasers WHITEBOOK*, edited by G. A. Mourou, G. Korn, W. Sandner, and J. L. Collier (THOSS Media GmbH, Berlin, 2011).
[22] M. H. Helle, D. Kaganovich, D. F. Gordon, and A. Ting, Phys. Rev. Lett. **105**, 105001 (2010).
[23] M. Schnell *et al.*, Nat. Commun. **4**, 2421 (2013).
[24] B. Dromey, *et al.*, Nat. Physics **8**, 804 (2012); D. an der Brügge and A. Pukhov, Phys. Plasmas **17**, 033110 (2010).
[25] A. G. R. Thomas *et al.*, Phys. Rev. Lett. **98**, 054802 (2007).